

Gravitational microlensing as a probe for dark matter clumps

E. Fedorova^{1,2*}, V.M. Sliusar², V.I. Zhdanov^{2†},
A.N. Alexandrov², A. Del Popolo^{3,4,5}, J. Surdej¹.

¹ *Institute of Astrophysics and Geophysics of Liège University, Quartier Agora Allée du 6 août 19C, B-4000 Liège, Belgium*

² *Astronomical Observatory of Taras Shevchenko National University of Kyiv, Observatorna 3, Kiev, 04053, Ukraine*

³ *Dipartimento di Fisica e Astronomia, University of Catania, Viale A.Doria 6, 95125, Catania, Italy*

⁴ *INFN sezione di Catania, via S.Sofia, 95123 Catania, Italy*

⁵ *International institute of physics, Universidade Federal do Rio Grande do Norte, 59012-970, Natal, Brazil*

ABSTRACT

Extended dark matter (DM) substructures may play the role of microlenses in the Milky Way and in extragalactic gravitational lens systems (GLSs). We compare microlensing effects caused by point masses (Schwarzschild lenses) and extended clumps of matter using a simple model for the lens mapping. A superposition of the point mass and the extended clump is also considered. For special choices of the parameters, this model may represent a cusped clump of cold DM, a cored clump of self-interacting dark matter (SIDM) or an ultra compact minihalo of DM surrounding a massive point-like object. We built the resulting micro-amplification curves for various parameters of one clump moving with respect to the source in order to estimate differences between the light curves caused by clumps and by point lenses. The results show that it may be difficult to distinguish between these models. However, some region of the clump parameters can be restricted by considering the high amplification events at the present level of photometric accuracy. Then we estimate the statistical properties of the amplification curves in extragalactic GLSs. For this purpose, an ensemble of amplification curves is generated yielding the autocorrelation functions (ACFs) of the curves for different choices of the system parameters. We find that there can be a significant difference between these ACFs if the clump size is comparable with typical Einstein radii; as a rule, the contribution of clumps makes the ACFs less steep.

Key words: astrophysics, cosmology – Gravitational microlensing, dark matter.

1 INTRODUCTION

Since the beginning of the last century, when some astronomers started to study the matter content of our neighborhood (Öpik 1932; Kapteyn 1922; Jeans 1923; Oort 1932; Zwicky 1933), many evidences have been collected leading one to believe that the Universe in which we live is mainly constituted by non-luminous matter, whose existence is inferred through its gravitational effects on the remaining constituents of the Universe. This “missing matter”, was dubbed “dunkle materie” (dark matter), by Zwicky (1933). Nowadays, we know, according to Plank’s data mission fitted with the Λ CDM model, that the Universe is composed

of 26.8% non-baryonic dark matter (DM) and 68.3% dark energy (represented by the Λ term), and just 4.9% ordinary matter (Ade et al. 2013). In this context, the role of Gravitational Lensing (GL) can hardly be overestimated. GL provides important evidences in favor of DM existence in galactic clusters (Markevitch et al. 2003; Clowe et al. 2004, 2006; Bradač et al. 2006). The other application of GL, following the idea by Paczyński (1986b), deals with the searches for compact objects in the Galactic halo and inside the Milky Way (Alcock et al. 1993; Udalski et al. 1993; Aubourg et al. 1993). GL effects over a wide range of lens masses can give us the possibility of analyzing the DM substructure characteristics; especially it can give us a clue to solve the “missing satellite” problem (Klypin et al. 1999; Moore et al. 1999; Del Popolo et al. 2014). Here we analyze the possibilities to

* ofedorova@ulg.ac.be

† valeryzhdanov@gmail.com

study some properties of DM using mainly photometric information induced by gravitational microlensing effects.

Following the terminology adopted by the GL community, at least three kinds of GL phenomena, characterized by different lens masses and typical timescales, exist:

- (i) macrolensing and the weak lensing by galaxies or groups of galaxies;
- (ii) mesolensing: lenses are globular clusters, dwarf galaxies or DM clusters with mass in the range 10^3 to $10^9 M_\odot$ (Baryshev & Bukhmastova 1997);
- (iii) microlensing: lenses are stellar-mass objects.

As distinct from (i) and (ii) dealing with almost static situations or very slow processes, the characteristic timescales of microlensing events in the Milky Way are of the order of weeks and in case of extragalactic microlensing events, they are of the order of months or years. This makes image brightness variation effects due to (iii) quite observable.

Based on the lens mass range/timescales, this terminology determines at the same time the possible observational appearance of these effects, i.e. multiple correlated static images with signal arrival time delays in the macrolensing case, slowly-varying distorted images due to mesolensing, and high amplification events on lightcurves when the source crosses the caustic of a microlens. Dark matter can manifest itself at the three mentioned levels, namely:

- (i) large haloes of DM with mass greater than $10^9 M_\odot$ can play the role of macrolenses; the most prominent example is the "Bullet Cluster" (Markevitch et al. 2003);
- (ii) DM subhaloes of intermediate masses can play the role of mesolenses, causing the anomalous flux ratios, image distortions (Chen et al. 2007) and additional time delays (Keeton & Moustakas 2009) in extragalactic gravitational lens systems. Several candidates to show anomalous flux ratios are known today, e.g., B2045+265 (McKean et al. 2007), RX J1131–1231, B1608+656, WFI 2033 – 4723 (Congdon et al. 2010), B1938+666 (MacLeod et al. 2012), and we would especially like to stress here the famous GLS Q2237+0305 for its sharp high-amplification microlensing events (Metcalf et al. 2003).
- (iii) Clumps of DM with stellar masses can play the role of microlenses, leading to both photometric (high amplification events) and astrometric (jump-like shifts of brightness centroid of the images of the microlensed source) appearances. The main difference between DM microlensing and the "usual" one due to stars or black holes lies in the non-negligible size of the DM clumps (non-DM microlenses are always considered as point masses).

In this paper, we pay attention to the last item, i.e. microlensing by extended clumps of stellar masses. We note that continuous observations by EROS, OGLE and other groups (Tisserand et al. 2007; Wyrzykowski et al. 2009) neither revealed any sign of these extended clumps in the Galactic halo, nor provided any proof of such structures inside the Galaxy. The overwhelming majority of the light curves observed for Galactic microlensing events are well described by the gravitational field of stars (and, sometimes, of planetary mass objects). Therefore, it seems that there is no room for the stellar mass extended clumps. However, in this paper we show that the light curves due to extended clumps of stellar

mass objects can mimic the light curves caused by ordinary compact objects. Therefore, more detailed investigation is needed in order to rule out (or to confirm) the existence of these DM clumps that may either not be very numerous (so that we do not have these clumps within our Solar system) or not so dense to be observable.

Photometric signatures of DM substructure via gravitational microlensing have been widely discussed; see Mao et al. (2004); McKean et al. (2007); Oguri (2005) and references therein. There are also some investigations of variability of spectral line profiles (Metcalf et al. 2003). Paczyński & Wambsganss (1989) derived amplification distributions for static gravitational macro-lensing with a non-constant surface mass density, which includes the cases of a stochastic system of Gaussian clumps and clumps in the form of truncated singular isothermal spheres. Zakharov & Sazhin (1999), and Zakharov (2010) have considered a model of microlensing due to a non-compact neutralino star.

In this paper we use several other models of DM clumps to analyze the observational appearance of DM microlensing within different cosmological models. We focus our attention on item (iii) to compare the observational appearances of microlensed sources due to point-like and finite-size DM clump deflectors and determine how one can distinguish an extended DM clump microlensing event from a "regular" one in case of Galactic and extragalactic structures. The main question we want to answer concerns the possibilities to detect signals from these putative extended mass structures and to estimate the accuracy needed to characterize such effects mainly from observed light curves.

In Section 2, we briefly describe the existing DM models. In Section 3, we propose a "toy model", which describes, for special choices of the parameters, microlensing by various types of extended structures. The model is based on the deflection angle $\alpha \sim \mathbf{r}(r^2 + r_s^2)^{-a/2}$, where r_s characterizes the effective size of a clump core¹. For different choices of parameters, this model reproduces the effects either due to point microlenses, or CDM minihaloes with a cusped density profile, or SIDM clumps with a cored density profile. In Section 4 we discuss the superpositions of extended and point-mass deflecting objects. In the case of isolated microlenses these models can be used to describe microlensing events within the Galaxy.

We perform a numerical comparison of these events considering different microlens models. Namely, we calculate the "amplification curves", that is the dependence of the total amplification of a microlensing system versus time, as the lens moves with respect to the line-of-sight to the source. We also pay some attention to the trajectories of the brightness centroid of the microlensed images, because the fast progress in the positional accuracy measurements² gives us a hope to detect the astrometric signatures of gravitational microlensing in the near future.

¹ The corresponding surface mass density is $\rho \sim (1 - a/2)(r^2 + r_s^2)^{-a/2} + (a/2)r_s^2(r^2 + r_s^2)^{-(1+a/2)}$

² e.g., projects of radio interferometry in space. Note that astrometric accuracy is typically several times larger than the resolution; i.e. one can achieve a microarcsecond level in positioning, though different images of the microlensed source cannot be resolved at this level.

In Section 5 we consider the observational behavior of clumps in extragalactic GLSS. Namely, we study the statistical effects of gravitational microlensing due to a stochastic system composed of extended DM clumps and point masses. There is a number of papers dealing with statistical subjects of microlensing systems; see, e.g., Schneider et al. (1992); Seitz et al. (1994); Neindorf (2003); Dobler et al. (2007); Schmidt & Wambsganss (2010). Our technique is essentially the same as that used by Paczyński & Wambsganss (1989) and Wambsganss et al. (1990), followed by a number of authors; cf. especially considerations by Metcalf & Madau (2001); Chiba (2002); Dalal & Kochanek (2002); Schechter & Wambsganss (2002) dealing with brightness variations in connection to the problem of anomalous brightness ratios. Unlike in the previous works we deal with the autocorrelation functions (ACFs) of the amplification curves for our concrete model of a microlensing system. We generate an ensemble of amplification curves for a fixed input of randomly distributed clumps and point mass microlenses in the total optical depth; this enables us to derive ACFs for these amplification curves as a function of different clump contribution, size and in presence of an external shear. Finally, in Section 6 we discuss the results.

2 PROPERTIES OF VARIOUS DM MODELS

DM microstructure still remains the subject of debates; there are many hypotheses about DM particles (Schneider & Weiss 1987; Zackrisson & Riehm 2010). Cold dark matter is supposed to contain heavy particles, weakly interacting with each other and with baryonic matter (axions or WIMPs), and warm dark matter (WDM) consists of light, fast-moving particles (sterile neutrinos, CHAMPs, neutralinos or gravitinos), which tend less to form small-scale compact structures (Schneider et al. 2012; Del Popolo 2014). Self-interacting dark matter can be considered as a particular kind of cold one with a nonzero impact distance for the interaction between DM particles (Kormendy & Freeman 2003; Rocha et al. 2012).

Recent cosmological N-body simulations within CDM (Schneider et al. 2010; Diemand et al. 2004, 2005; Springel et al. 2008; Stadel et al. 2009; Vogelsberger et al. 2012) and WDM models (Knebe et al. 2008; Schneider et al. 2012) have shown that dark matter is not distributed in space homogeneously, instead it forms more or less compact structures surrounded by less dense continuously distributed DM. The most massive structures have been recognized for quite a long time already: these are galactic and galaxy cluster DM haloes. But numerical simulations demonstrate that these massive structures are also inhomogeneous: they contain smaller compact substructures over a wide range of masses. Such massive haloes containing a hierarchical substructure of dark matter are called host haloes. These haloes also contain smaller substructures, etc. However, one should note that only the existence of the more massive members of this hierarchy of DM structures has been proven from the results of observations. The lower estimated limit on the substructure masses depends on the particular kind of considered hypothetical DM particles, varying over a very wide range from $10^{-12}M_{\odot}$ for CDM up to 10^8M_{\odot} for

Table 1. Dark matter hierarchy within the CDM/SIDM cosmologies.

Term	Objects/scales	Mass range
Superhalo	Galaxy clusters, 100 Mpc	10^{13} - $10^{16}M_{\odot}$
Halo	Galaxies, Mpc	10^9 - $10^{11}M_{\odot}$
Subhalo	Dwarf galaxies or satellites, kpc	10^4 - 10^9M_{\odot}
Minihalo or clump	Stars	10^{-3} - $10M_{\odot}$
Microhalo	Planets	10^{-8} - $10^{-4}M_{\odot}$
Nanohalo or primordial halo		10^{-18} - $10^{-9}M_{\odot}$

WDM (Berezinsky et al. 2008, 2013; Diemand et al. 2005; Springel et al. 2008). To clear out the situation and the terminology used to characterize masses and scales of DM substructures, we have summarized here in Table 1 the used nomenclature.

DM substructure depends very significantly on the cosmological model. Within CDM models, the substructure formation process can be described as “bottom-up”: the smallest DM clumps were formed first (therefore the nanohaloes with masses $< 10^{-11}M_{\odot}$ are often referred as primordial) and do not contain any finer substructure (Contini et al. 2011). Then, in the merging process more and more massive structures up to galactic and cluster scales (10^{10} - $10^{15}M_{\odot}$) were gradually formed. Due to various damping scales the lower limits on substructure mass can vary over a wide range: from 10^{-4} - $10^{-12}M_{\odot}$ for various kinds of WIMPs (including neutralinos), down to 10^{-18} - $10^{-20}M_{\odot}$ for axions. The mass density distribution in DM structures within the CDM model is often assumed to follow the cusped NFW profile of Navarro et al. (1996).

The best accepted alternative to the CDM cosmology is the velocity-dependent SIDM (self-interacting-dark-matter). This model predicts identical behavior of the DM substructure over various scales and identical mass fractions, thus, the only difference lies in the density profile of a DM clump. The SIDM clump has a core and its density follows a Burkert profile (Rocha et al. 2012), or pseudo-isothermal sphere (Kormendy & Freeman 2003), contrarily to the cuspy coreless NFW profile typical for CDM clumps.

The set of warm dark matter models differs completely from the two mentioned above when we keep in mind gravitational microlensing processes. The substructure formation in WDM models is a complex hybrid; its leading role is played by the “top-down” formation process (Knebe et al. 2008), i.e. bigger haloes and filaments were formed first, and smaller structures formed later, as a result of fragmentation processes in WDM filaments (Knebe et al. 2003). The lower limit on the subhalo mass is significantly higher than in CDM/SIDM ones: e.g., $10^6 - 10^8M_{\odot}$ for gravitinos and even $10^{11}M_{\odot}$ for axinos (Hisano et al. 2006). Thus in the WDM cosmology, we may predict the non existence of DM gravita-

tional microlensing. Even despite that it was recently shown (Paduroiu et al. 2015) that the WDM structure formation rather follows the hybrid scenario than the “top-down” one, the effects of fragmentation and collapse play a significant role only in massive haloes formation, and thus the situation with dark matter induced gravitational microlensing in WDM cosmology is not significantly altered.

The DM subhalo mass function (SHMF) $n(m, M_0)$, such that $n(m, M_0)dm$ represents the space number of substructures with a mass in the range $\{m, m + dm\}$ in the host DM halo with a mass M_0 is strongly sensitive to the DM context (i.e. warm, cold, collisionless, repulsive and so on). The SHMF appears to provide the essential source of crucial information both in cosmology and elementary particle physics. The numerical simulations like “Millennium” (Springel et al. 2005) or “Via Lactea” (Contini et al. 2011) allow us to determine it only at higher subhalo masses (mainly $> 10^6 M_\odot$) than typical microlens masses (i.e. not greater than $100 M_\odot$). However for lower masses of the substructure we can use here the extrapolated mass function obtained by Lee et al. (2009):

$$f(m) = 0.1 \frac{\log(M_{max}/m)}{\log(M_{max}/M_{ch})}$$

where $M_{max} = 0.01 M_\odot$ and $M_{ch} = 10^7 M_\odot$. Thus, the total mass in substructures within the CDM model (with a lower limit of $10^{-6} M_\odot$) is 52%, following Lee et al. (2009). This value is in good agreement with the 50% of dark matter in the Galactic halo in substructures obtained from the hydrodynamical simulations by Diemand et al. (2004). Using this formula, one can easily find that for the lower limit of $10^{-3} M_\odot$ (which can be considered as a reasonable limit for microlens mass) it is 43%, and for $10 M_\odot$ (let us consider this value as an upper limit on microlens mass) it is 30%. Thus within the desirable range ($10^{-3} - 10$) M_\odot of the substructures we have 13% of the total DM mass (i.e. $\sim 1.3 \cdot 10^{11} M_\odot$ is in compact stellar-mass subhaloes). If we take into account the fact that the larger subhaloes (with mass greater than $10 M_\odot$) also contain finer substructures, this value can be even larger.

However, estimating the probability of the DM subhalo microlensing we should take into account that up to 90% of the primordial subhaloes had to be fully or partially disrupted by tidal forces of stars, thus the percentage of the clumped matter in the areas containing stars cannot exceed 10% (Schneider et al 2011; Schaw et al. 2007). Thus we can expect to trace the DM-induced high amplification microlensing events in the Galactic DM halo (as well as in extragalactic systems) rather than in its luminous parts. The probability of the Galaxy stars being microlensed by a DM microhalo is much lower then. That is why we can hardly expect to find compact DM clumps in the vicinity of the Solar system.

However, at the same time, in the luminous parts of a galaxy we can face the situation when a star (or a star-mass black hole) is surrounded by a dense cloud, formed by dark matter of a former clump, disrupted by star/black hole tidal force and trapped by its gravity. If such a clump is dense enough and thus has an optical depth large enough (overcritical convergence), we can observe the UCMH (Zhang 2011; Berezhinsky et al. 2013), and one of the possible results of gravitational microlensing by such an object looks

like an eclipse of the source image. The role of optical depth/convergence in microlensing processes was analyzed by Paczyński (1986a). In the simplest case such an object can be modeled up by a Schwarzschild or Chang-Refsdal lens with overcritical convergence.

3 EXTENDED CLUMP MICROLENSING IN THE GALAXY

3.1 The lens equation

Speaking about the Milky Way systems, we confine ourselves to the simplest cases of circular symmetric mass distributions though investigations of double stars or planetary systems are also important. One can get some insight into the latter case from considerations of clump models with an external shear (Sliusar et al. 2015). In this Section, we use the lens equation in its normalized form; the distances will be expressed in units of a typical length scale R_* , where for the case of the point mass M or cored clump microlens $R_*^2 = 4GM D_{ds}/(c^2 D_d D_s)$ (in case of a point mass this is the radius of the Einstein ring) and for the cusped clump $R_*^a = 8\pi G \rho_0 D_{ds}/[c^2 D_d D_s(2-a)]$; here D_s is the distance between the source and the observer, D_d the distance between the deflector and the observer, and D_{ds} the distance between the source and the deflector. Furthermore \mathbf{y} is the normalized angular source position, $\mathbf{r} = \{x_1, x_2\}$ is the normalized angular image position, $r = |\mathbf{r}|$. We remind here that (after normalization) both these vectors are defined in the lens plane.

The normalized lens equation is:

$$\mathbf{y} = (1 - \sigma) \mathbf{r} - \alpha(\mathbf{r}), \quad (1)$$

where the deflection angle

$$\alpha(\mathbf{r}) = \frac{\mathbf{r}}{r^2} \int_0^r dr' r' \rho(r') \quad (2)$$

is supposed to be normalized to a corresponding length scale, $\sigma = const$ stands for a convergence (optical depth) that can be due to, e.g., a background DM; $\mathbf{y} = \{y_1, y_2\}$.

Let us write $\alpha(r) = \mathbf{r}/r^a$, where for the cusped clump we assume $a < 2$ to provide the convergence in the integral of Eq.(2), and for the point microlens $a = 2$. For the cored clump we use a generalized expression $\alpha(\mathbf{r}) = \mathbf{r}/(r^2 + r_s^2)^{a/2}$ that formally covers the previous cases if we put $r_s = 0$. Therefore, we consider the lens equation

$$\mathbf{y} = \mathbf{r} (1 - \sigma - R^{-a}), \quad R = \sqrt{r^2 + r_s^2}, \quad a > 0. \quad (3)$$

The determinant of the lens mapping (3) is $D = \det\{\partial y_i / \partial x_j\}$. It factorizes as follows:

$$D(r) = \varphi_1(r) \varphi_2(r), \quad (4)$$

where

$$\varphi_1(r) = 1 - \sigma - \frac{1}{R^a}, \quad \varphi_2(r) = 1 - \sigma + \frac{a-1}{R^a} - \frac{ar_s^2}{R^{a+2}}. \quad (5)$$

The image parity is defined by the sign of D .

The relative amplification³ of the image at \mathbf{r} is $\mu(\mathbf{r}) = (1 - \sigma)^2 / |D(r)|$.

³ this is normalized to the amplification $(1 - \sigma)^2$ when the source is far from the lens.

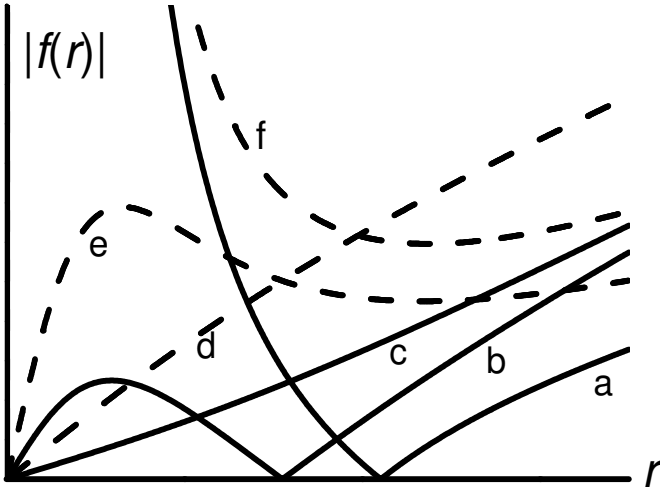


Figure 1. Qualitative behavior of the r.h.s. of Eq. (6) for the subcritical case ($0 \leq \sigma < 1$: solid; a,b,c) and the overcritical case ($\sigma > 1$: dashed; d,e,f). Here we show the subcritical cases (a) $a > 1, r_s = 0$, (b) $0 < r_s < r_{s,cr}$, (c) $r_s > r_{s,cr}$; in case of (b) and (c) there may be an inflection point that does not affect the number of images. The overcritical cases: (d) $0 < a < 1$; (e) $a > 1, r_s < r_{s,cr1}$; (f) $r_s = 0, a > 1$.

Taking the absolute value of both sides of Eq. (3) yields

$$y = |f(r)|, \quad (6)$$

where $f(r) \equiv r[1 - \sigma - (r^2 + r_s^2)^{-a/2}]$, $y = |\mathbf{y}|$. Evidently, if r is a solution of Eq.(6), then the solution of Eq.(3) is either $\mathbf{r} = \mathbf{n}_y r$ or $\mathbf{r} = -\mathbf{n}_y r$, where $\mathbf{n}_y = \mathbf{y}/y$.

Our first goal will be to estimate the number of solutions of Eq.(3), i.e. the number of microlensed images for different source positions, and to find the caustics of the lens mapping (3) where the lensed image of a point-source gets infinitely amplified. The problem is reduced to investigate the monotonicity of the r.h.s. of Eq. (3) and the zeros of the determinant $D(r)$ in Eq. (4). Note that any root of $\varphi_2(r)$, if it exists, is smaller than the root of $\varphi_1(r)$ (for $a > 0$) because of the monotonicity of $\varphi_1(r)$ and due to $\varphi_2(r) = \varphi_1(r) + ar^2/R^{a+2}$.

Simple calculations yield

$$\frac{df(r)}{dr} = \varphi_2(r), \quad \frac{d\varphi_2(r)}{dr} = -\frac{ar}{R^{a+4}} [(a-1)r^2 - 3r_s^2], \quad (7)$$

whence for $a > 1, r_s > 0$ we infer the existence of the only inflection point $r_{infl} = r_s \sqrt{3/(a-1)}$ of the curve $y = f(r)$ and there is no inflection for $a < 1$.

3.2 Cored clump, subcritical σ

Let us first consider the case $r_s \neq 0$ and the subcritical values of σ : $0 \leq \sigma < 1$. Further we denote $r_{s,cr} = (1-\sigma)^{-1/a}$.

For the case $r_s < r_{s,cr}$, the first factor $\varphi_1(r)$ of the r.h.s. in Eq. (4) equals zero for $r = r_z \equiv [(1-\sigma)^{-2/a} - r_s^2]^{1/2}$. This corresponds to a circular critical curve with a radius r_z around the origin of the image plane, which is mapped onto an isolated caustic point $\mathbf{y} = 0$ in the source plane. Thus, there is a solution for Eq. (3) with $\mathbf{y} = 0$. For $r_s > r_{s,cr}$ the function $\varphi_1(r)$ is always positive.

For the second factor $\varphi_2(r)$ in Eq. (4) we also have the condition⁴ $1 - \sigma < r_s^{-a}$ (i.e. $r_s < r_{s,cr}$) for the existence of $r_c < r_z$ such that $\varphi_2(r_c) = 0$. Indeed, under this condition, $\varphi_2(0) = 1 - \sigma - r_s^{-a} < 0$ and $\varphi_2(r_z) > 0$ have different signs. This is a necessary and sufficient condition for a unique value of r_c to exist on $(0, r_z)$. The proof of the uniqueness is somewhat different for $0 < a < 1$ and $a > 1$. For $0 < a < 1$ the function $\varphi_2(r)$ is monotonically increasing. For $a > 1$ one should use Eq. (7) and take into account the existence of the unique inflection point for f : we observe that $\varphi_2(r)$ is monotonically increasing for $r < r_{infl}$ (therefore there can be only one zero in this region provided that $r_s < r_{s,cr}$); after passing through a maximum at $r = r_{infl}$ it decreases and it is positive: $\varphi_2(r) > \varphi_2(\infty) = 1 - \sigma > 0$.

It is easy to see that $r_c < r_z$, when it exists, is the radius of a circular critical curve that is mapped onto a circular caustic with radius $y_c = |f(r_c)|$. There exist two additional images of a point source for the case $y < y_c$. The problem can be easily treated using the graph of $|f(r)|$ (Fig. 1, b,c) and taking into account the fact that $d|f|/dr$ is either equal to $-\varphi_2$ or to φ_2 . For $r_s > r_{s,cr}$ the function $|f(r)|$ starting at $r = 0$ is monotonically increasing, therefore, for any \mathbf{y} there is a unique solution $r(y)$ of Eq. (6). The (unique) solution of Eq. (3) is $\mathbf{r} = \mathbf{n}_y r(y)$ having positive parity.

For $r_s < r_{s,cr}$ we have $f(r) < 0, r \in (0, r_z)$. The function $|f(r)|$ has only one maximum $y_c = |f(r_c)|$. For $r > r_z$ the r.h.s. of (Eq. 6) is a monotonically increasing function. Therefore, for $0 < y < y_c$ there are three solutions for Eq. (6): two solutions $r = r_i \in (0, r_z), i = 1, 2; r_1 < r_2$, which yield two solutions of the vectorial lens equation (3) $\mathbf{r} = -\mathbf{n}_y r_i$ (r_1 with positive parity, r_2 with negative parity); and one solution $r_3 > r_z$ yielding the solution $\mathbf{r} = \mathbf{n}_y r_3$ with positive parity for Eq. (3).

To sum up, for $0 \leq \sigma < 1$ we have a unique image for the case $r_s > r_{s,cr}$; in addition, for $y = 0$ there is an image⁵ at $r = 0$. All images have a finite brightness. In the opposite case, for $0 < r_s < r_{s,cr}$ there is a circular caustic with radius $y = y_c$ and there are three images, if the source is inside this caustic $0 < y < y_c$, and one image, if $y > y_c$. Two images acquire an infinite amplification when $y \rightarrow y_c - 0$ and then disappear after crossing y_c . In addition, there is a caustic ring emerging in case of a point mass lens.

The caustics with source tracks and corresponding amplification curves are shown in Fig.2.

3.3 Cored clump, overcritical σ

For $\sigma > 1$ ($r_s \neq 0$), let us first consider the case $0 < a < 1$. In this case in equation (6) $|f(r)| \equiv r[\sigma - 1 + (r^2 + r_s^2)^{-a/2}]$ is a monotonically increasing function (see Fig. 1, d, dashed curve). Its derivative is $d|f(r)|/dr = -\varphi_2(r) > \sigma - 1 > 0$. The lens mapping has no caustics and critical curves; for any \mathbf{y} there is always a unique solution r for Eq.(6) and a unique solution $\mathbf{r} = -\mathbf{n}_y r$ (positive parity) for the vectorial lens equation (3).

⁴ This condition is formally the same as the one for the existence of a root of $\varphi_1(r)$

⁵ for completeness, we note that the trivial solution $\mathbf{r} = 0$ for $\mathbf{y} = 0$ exists, if $r_s \neq 0, \forall a > 0$, and if $r_s = 0, a < 1$.

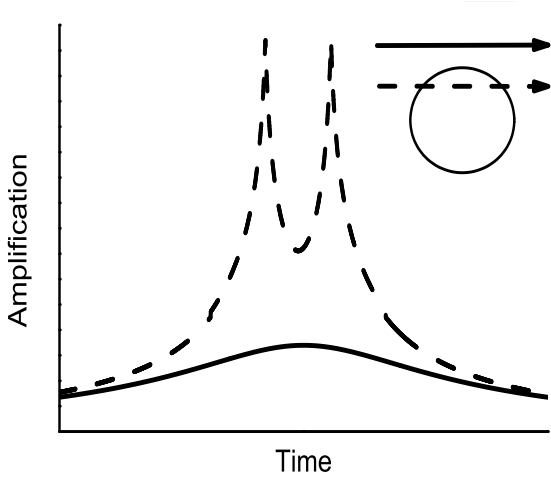


Figure 2. Qualitative behavior of the amplification curves, the subcritical case, $0 < r_s < r_{cr}$. The upper curve (dashed): the point source moves along the straight line with the impact parameter $y < y_c$ yielding two caustic crossings. The lower curve (solid): larger $y > y_c$, no caustic crossings. In the right upper corner: the trajectories with respect to the circular caustic of the lens.

For $\sigma > 1$, $a > 1$ there is an inflection point of the function $|f(r)| \equiv -f(r)$ according to Eq. (7). Taking into account the sign of this inflection, we see that there exists a minimum for $d|f(r)|/dr$ at $r = r_{infl}$, which is equal to

$$f'_{min} = \sigma - 1 - \frac{2}{r_s^a} \left(\frac{a-1}{a+2} \right)^{a/2+1}.$$

Then new roots of $d|f(r)|/dr$ appear when

$$r_s < r_{s,cr1} = \left(\frac{2}{\sigma-1} \right)^{1/a} \left(\frac{a-1}{a+2} \right)^{(a+2)/(2a)}.$$

If $r_s \geq r_{s,cr1}$, the function $|f(r)|$ is monotonically increasing (not shown in Fig. 1). Let these new roots be $r_{c,1}$ and $r_{c,2}$ with $r_{c,1} < r_{c,2}$, $r_{c,1}$ being a point of a local maximum of $|f(r)|$ and $r_{c,2}$ being a point of a local minimum (see Fig. 1, e, dashed). The roots correspond to the radii of the critical curves, and $|f(r_{c,1})|, |f(r_{c,2})|$ are the radii of the circular caustics. For $|f(r_{c,1})| < y < |f(r_{c,2})|$ Eq.(6) has three solutions $r_1 < r_2 < r_3$ correspondingly with a positive, negative and positive parity yielding three lensed images of a point source, and there is only one image with positive parity otherwise. The solution $r_1(y)$ is extended for $y < |f(r_{c,1})|$ and the corresponding image has an infinite amplification when $y \rightarrow |f(r_{c,1})| - 0$; in this case $r_1(y)$ and $r_2(y)$ tend to $r_{c,1}$ and then disappear after y crosses the value $|f(r_{c,1})|$. The solution $r_3(y)$ is extended to all values of $y > |f(r_{c,2})|$; it has analogous properties near the other caustic for $y \rightarrow |f(r_{c,2})| + 0$. In this case $r_2(y)$ and $r_3(y)$ tend to $r_{c,2}$ and then disappear as y decreases. We have for the solutions of Eq.(3), $\mathbf{r} = -\mathbf{n}_y r_i$, $i = 1, 2, 3$.

3.4 Cusped clump: $r_s = 0$

Here we have $f(r) = r(1 - \sigma - r^{-a})$. For $0 < \sigma < 1$, the function $f(r) < 0$ for $r < r_{z1} = (1 - \sigma)^{-1/a}$; r_{z1} is the radius of a critical curve corresponding to the caustic point $y = 0$.

For $0 < \sigma < 1$ and $0 < a < 1$, the modulus $|f(r)|$

increases for $r < r_{max} = [(1 - a)/(1 - \sigma)]^{1/a}$ and then decreases to zero for $r \rightarrow r_{z1}$. The value $y_c = |f(r_{max})| = a[(1 - a)/(1 - \sigma)]^{1/a-1}$ is the radius of a circular caustic. The behavior of the graph of this function is roughly the same as that illustrated by the solid curve in Fig. 1, b. There are three solutions for Eq. (6) with $0 < y < y_c$: namely, two solutions r_i , $i = 1, 2$, $r_1 < r_2$ for Eq. (6), $r_i < r_{z1}$ corresponding to images at $\mathbf{r} = -\mathbf{n}_y r_i$ (with positive (r_1) and negative (r_2) parity, and one solution $r_3 > r_{z1}$ corresponding to image at $\mathbf{r} = \mathbf{n}_y r_3$ with positive parity. The latter solution remains valid for $y > y_c$.

For $0 < \sigma < 1$, $a > 1$, the function $f(r)$ is negative for $r \in (0, r_{z1})$, the modulus $|f(r)|$ decreases along this interval and it increases for $r > r_{z1}$. The behavior of $|f(r)|$ is represented by the curve (a) in Fig. 1. In this case there are always two solutions of Eq. (6) for $r_1 < r_2$ corresponding to images at points $\mathbf{r} = -\mathbf{n}_y r_1$, $\mathbf{r} = \mathbf{n}_y r_2$.

For $\sigma > 1$ and $0 < a < 1$ the function $|f(r)|$ increases for all values of $r > 0$ starting from zero (like the dashed curve (d) in Fig. 1). There is only one solution and one image for all y values.

For $\sigma > 1$ and $a > 1$ the function $|f(r)|$ shows a minimum at $r_{min} = [(a - 1)/(\sigma - 1)]^{1/a}$; the minimum is $y_c = |f(r_{min})| = a[(\sigma - 1)(a - 1)]^{1-1/a}$ (the radius of a circular caustic). There are two solutions for Eq. (6) if $y > y_c$ and no solutions if $y < y_c$. This case is represented by the dashed curve (f) in Fig. 1.

3.5 Analytical solutions

In this subsection, we list several situations whenever a simple analytical treatment is possible.

The point mass lens model (Schwarzschild lens) is well known, it corresponds to $a = 2$, $r_s = 0$, $\sigma = 0$. The solutions for the image positions are $\mathbf{r} = \mathbf{y}(y \pm \sqrt{y^2 + 4})/2y$ and the total amplification of the two lensed images is $\mu = (y^2 + 2)/(y\sqrt{y^2 + 4})$.

For a single SIDM cored clump, let us assume $a = 2$, $\sigma = 0$: critical curves for such a system exist only when $r_s < 1$. Under this condition, two circular critical curves exist. The first one has a radius $r_z = \sqrt{1 - r_s^2}$ corresponding to the caustic point $y = 0$ (the same as for the point-mass lens), and the second one has a radius r_c such that $r_c^2 = \frac{1}{2}(\sqrt{1 + 8r_s^2} - 1) - r_s^2 < r_z^2$ (this expression is positive for $r_s < 1$), corresponding to a caustic with a radius $y_c = r_c(1 - r_c^2 - r_s^2)/(r_c^2 + r_s^2)$. In case of a cored clump microlens, the lens equation yields: $r^3 \mp y r^2 + r(r_s^2 - 1) \mp y r_s^2 = 0$. The roots can be found using the Cardano method. For the lower plus, two roots must be taken in the interval $0 < r < r_z$ for $y < y_c$, and for the upper minus, one must take the root for $r > r_z$. If $r_s > 1$ (low-density clump), no caustic exists and only one lensed image can be seen.

For the UCMH model, it is interesting to consider an analytic solution for the overcritical case $\sigma > 1$ ($r_s = 0$, $a = 2$). In this case there exists a critical curve $r_c = 1/\sqrt{\sigma - 1}$ and the radius of the corresponding caustic is described by $y_c = 2\sqrt{\sigma - 1}$. Two images for $y > y_c$ are produced at the positions: $\mathbf{r} = -\mathbf{y}[y \pm \sqrt{y^2 - 4(\sigma - 1)}]/[2y(\sigma - 1)]$. The total amplification of these two lensed images is $\mu = [y^2 - 2(\sigma - 1)]/[y\sqrt{y^2 - 4(\sigma - 1)}]$. For $y < y_c$ there are no images and we have an "occultation". The lightcurves cor-

responding to this effect, both for point-like and continuous sources, were shown in our previous work (Fedorova et al. 2014).

For the case of the cusped lens model, the solutions can be written analytically for $a = 3/2$. The lens equation $\mathbf{y} = \mathbf{r} (1 - r^{-3/2})$ has two solutions. The first solution must be written separately for $\xi = 3\sqrt{3}/(2y^{3/2}) < 1$ and $\xi > 1$:

$$\mathbf{r} = \frac{\mathbf{y}}{3} \frac{\left[\left(\xi + \sqrt{\xi^2 - 1} \right)^{2/3} + 1 \right]^2}{\left(\xi + \sqrt{\xi^2 - 1} \right)^{2/3}}, \quad \xi > 1;$$

and

$$\mathbf{r} = \frac{4}{3} \mathbf{y} \cos^2 \left[\frac{1}{3} \arccos \xi \right], \quad \xi < 1.$$

The second solution is

$$\mathbf{r} = -\frac{\mathbf{y}}{3} \frac{\left[\left(\xi + \sqrt{\xi^2 + 1} \right)^{2/3} - 1 \right]^2}{\left(\xi + \sqrt{\xi^2 + 1} \right)^{2/3}}$$

for any value of y . The magnification curves for these images can be found using the formula (4): $\mu = \left| (1 - 1/r^{3/2}) (1 + 1/(2r^{3/2})) \right|^{-1}$.

4 COMPARISON BETWEEN THE CLUMP MODELS AND THE POINT MASS LENS

4.1 Observational mimicry of the extended mass microlenses and the source image tracks

How can one distinguish between the different lens models discussed above on the basis of observations? Of course, the most correct comparison must come after the fitting of concrete observational data. However, let us first note the qualitative differences mainly arising from the topological properties of the corresponding lens mappings, i.e. the existence of the critical curves, caustics and number of images of a point source. From the above discussion it is easy to see that, for different parameters of the source/lens motion, the caustic intersections can occur leading to appearances/disappearances of the lensed images. These events could lead to such observable effects as high amplifications of the lensed image flux, "occultations" and sudden jumps of the average image positions (image centroids).

There exist many observational data compiled by EROS, OGLE and other groups (Tisserand et al. 2007; Wyrzykowski et al. 2009) hunting for microlensing events caused by Galactic objects.

Some of these events show a complicated behavior like those characteristic of caustic crossings. This is typically related to the existence of double star systems or planetary systems (Kains et al. 2013; Shin et al. 2007). However, most typical HAEs (Tisserand et al. 2007; Wyrzykowski et al. 2009) can be interpreted using the isolated point mass lens model. It is important to note that there exist some high amplification events with no detector identified.

On the other hand, for most of the events the deflector-star has been identified; however this case does not rule out

the situation (discussed below) when an extended clump surrounds the star. Correspondingly, at this stage we concentrate on the most simple models of extended microlenses; and we choose the parameters of their motion without caustic crossings. Namely, we consider the clump models with two lensed images that will be compared with the "fiducial" model of the usual point mass microlens (the Schwarzschild lens). For Galactic systems we assume the background continuous matter density to be $\sigma = 0$. The critical curves of the two-image clump models appear to be very similar in case of the Schwarzschild microlens and the cusped clump with $0 < \sigma < 1$ and $a > 1$. In these cases there is one circular critical curve of unit radius; and also, one caustic point at $y = 0$ exists. The case of a cusped clump with $a < 1$ is topologically different, however it will be also difficult to distinguish its light curve from that due to the Schwarzschild lens.

Below we show amplification curves generated with different models corresponding to a straight line motion of the microlensing system with respect to the line-of-sight towards the remote point source. It turns out that the shape of the amplification curves induced by two-image clumps are qualitatively similar to the ones induced by a Schwarzschild microlens, and thus they can hardly be distinguished from one another. Indeed, by an appropriate choice of the impact parameter and the velocity with respect to the line-of-sight, the Schwarzschild lens light curve can be well fitted by microlensing due to a cusped clump (see Fig. 3). For a wide range of parameters that may be considered as typical for this problem, the difference between the amplification curves on a plot is sometimes not visible to the eye. One can extract an additional information from the image centroid (IC)⁶ tracks in the reference frame of the source (see Fig. 3, lower panel). This, however, requires an accuracy for the positioning measurements at the microarcsecond level; this is typical for microlensing by Galactic objects and is not accessible at present. E.g., the modern accuracy achieved with HST (WFPC3 camera) is around 20-40 microarcseconds (Riess et al. 2014).

4.2 Numerical estimates

Thus, we proceed in more detail with the differences between the amplification curves corresponding to different microlens models. Note that we performed a fitting of the amplification curves in Figs. 3, 4, 5 so as to provide the best overlapping near the maximum of the curves (where they can be well approximated by a parabola, and where one can expect a good measurement accuracy). Careful inspection of these figures shows that there is a slight deviation between the curves in the wings of the separate HAEs. In this connection, to compare the different microlens models, we proceed as follows.

For a moving extended microlens characterized by an impact parameter p with respect to the line-of-sight, and a transverse velocity (assumed to be $V = 1$), we generate

⁶ The image centroid here is a weighted average of positions of all the images (with the exception of the lenses that we assume to be not visible); the weights are proportional to the amplifications of the corresponding lensed images.

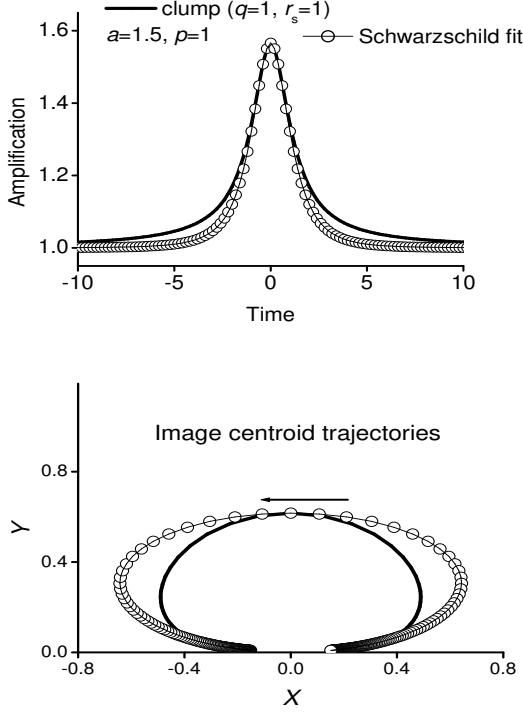


Figure 3. Amplification curves (upper panel) and image centroid trajectories (lower panel) for the cases of a cored clump (solid) and a point mass microlens (marked by the small circles). The clump parameters shown in the figure correspond to Eq. (9) ($q = 1$ corresponds to a pure clump, $p = 1$ is the impact parameter of the clump center with respect to the line-of-sight, its transverse velocity $V = 1$). The impact parameter and transverse velocity of the point mass microlens are derived from fitting the amplification curve for the clump model. The image centroid trajectory (in the rest frame of the source) in case of the Schwarzschild lens is rescaled in order to clearly indicate the difference between the models.

its amplification curve $\mu(t)$. Then we look for the best fit near the maximum of this curve using the Schwarzschild lens model light curve ($\mu_{Schw}(t)$); see Appendix A for details. Note that as distinct from dealing with the real observational data we have a simpler problem. In the real case, the fitting parameters, besides the transverse velocity and the impact parameter of the Schwarzschild lens (which are different from the assumed parameters p , $V = 1$ of the clump+point mass complex), are: the time of maximum amplification and the maximum intensity of the image (or the flux when the lens is far from the line-of-sight). In our case of the artificial amplification curve, the latter two parameters are fixed. Thus the difference between the two amplification curves is:

$$\delta = \max_t \{ [\mu(t)]^{-1} |\mu(t) - \mu_{Schw}(t)| \}. \quad (8)$$

This is used to compare the amplification curves due to a somewhat more complicated model which corresponds to a combination of a point mass microlens and an extended clump.

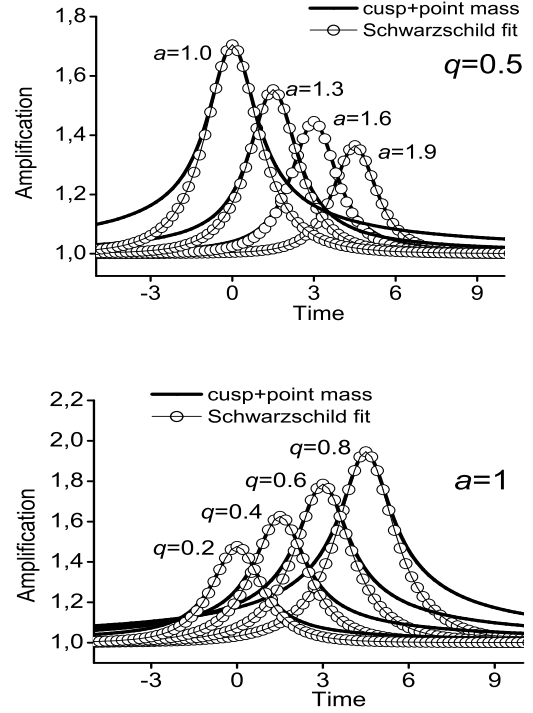


Figure 4. Examples of amplification curves (solid) for microlensing systems that consist of point masses surrounded by cusped clumps with $q = 0.5$, $a = 1.0, 1.3, 1.6, 1.9$ (upper panel) $a = 1$, and $q = 0.2, 0.4, 0.6, 0.8$ (lower panel). The impact parameter of the microlens with respect to the line-of-sight is $p = 1$. The curves are fitted by means of point mass microlens models (small circles).

4.3 Microlensing by a point mass and a clump

It is natural to consider a situation where the cusped or cored DM clump is formed in the same region as where the point mass is situated (and vice versa). The case of a pure clump microlens and the Schwarzschild lens represent two extreme cases of this situation. In this connection we consider a microlens model that is represented by the following lens equation:

$$y = r \left(1 - \frac{q}{R^a} - \frac{1-q}{r^2} \right), \quad R = \sqrt{r^2 + r_s^2}, \quad (9)$$

where the coefficient q describes the relative contribution of the clump, $1 - q$ represents that of the point mass lens, and we omitted the contribution due to the background optical depth σ ; $0 \leq q < 1$, $r_s > 0$. The amplification is $\mu(r) = 1/D(r)$, where the determinant $D(r)$ is also given by the product $D(r) = \varphi_1(r)\varphi_2(r)$ with

$$\varphi_1(r) = 1 - \frac{q}{R^a} - \frac{1-q}{r^2}, \quad (10)$$

$$\varphi_2(r) = 1 + \frac{q(a-1)}{R^a} - \frac{aqr_s^2}{R^{a+2}} + \frac{1-q}{r^2}. \quad (11)$$

Furthermore, we assume such numerical values for the parameters of the microlens as to provide the qualitative behavior of the lens mapping (9) to be like that of the Schwarzschild lens with two lensed images, and so as to provide a considerable amplification (up to 10 and

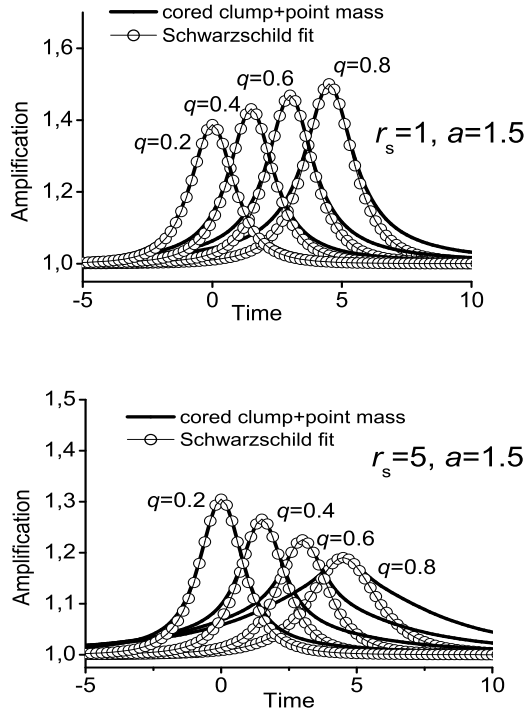


Figure 5. The same as in the lower panel of Fig. 4 for cored clump models with $a = 1.5$, $r_s = 1$ and $r_s = 5$. The impact parameter of the microlens with respect to the line-of-sight is $p = 1$.

higher), which can be the best to see the signals of the extended microlens structure. We shall then estimate the accuracy of measurements needed to differentiate between the lightcurves of these models. The dependence of this difference upon the contribution q of the clump in the lensing complex "cored clump + point mass" is shown in Fig. 6 for some values of a and r_s .

In case of the configuration of a point mass and a cusped clump we assume $q \in (0, 1)$, $r_s = 0$. The relative differences between the amplification curve of this complex and that of the fitted Schwarzschild lens are shown in Fig. 7.

5 STATISTICAL EFFECTS OF DM CLUMPS MICROLENSING IN EXTRAGALACTIC GLS

In a typical extragalactic GLS we have several macro-images of one quasar. Comparison of the amplification curves of these images makes it possible to separate the proper brightness variations of the quasar and to derive variations due to the microlensing processes. Contrary to the case of the Galaxy, because of the considerable microlensing optical depth in extragalactic systems, instead of an isolated point mass or putative DM clump, we must deal with an aggregate of masses in the lensing galaxy. In this case we have a complicated caustic network generated by unknown masses with unknown positions. Therefore, the problem takes a statistical shade (Paczynski & Wambsganss 1989; Wambsganss et al. 1990; Schechter & Wambsganss 2002). Observationally, the main source of information in a concrete GLS is at present an effective microlensed light curve

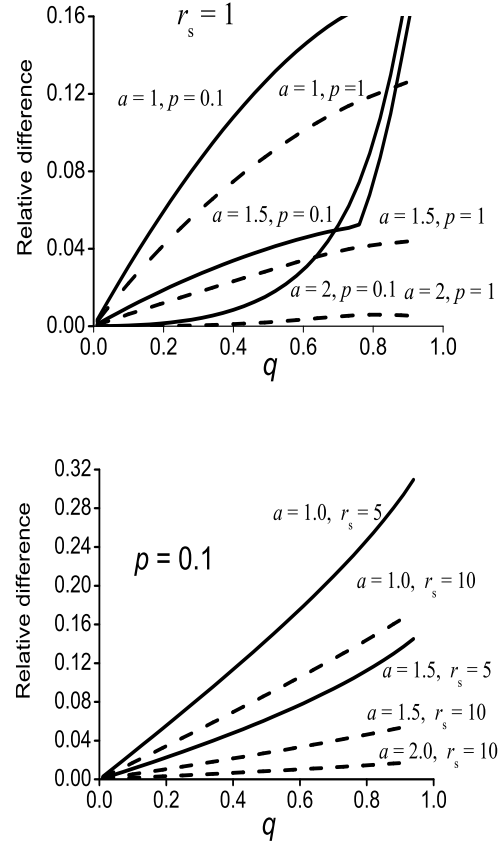


Figure 6. Relative differences δ of the amplification curves for a different cored clump contributions q in the microlensing complex "point mass + clump". Upper panel: $a = 1.0, 1.5, 2.0$, impact parameter $p = 0.1$ (solid curves), $p = 1.0$ (dashed curves), the clump size $r_s = 1$; the amplification is within the limits $\sim 10 \div 16$. For $p = 0.03$ we have almost the same curves as for $p = 0.1$, but the amplification in this case varies from ~ 30 to 50 . Lower panel: the same values of a , $p = 0.1$, $r_s = 5$ (solid), $r_s = 10$ (dashed). The curve with $a = 2$, $r_s = 5$ is superimposed on the curve with $a = 1.5$, $r_s = 10$ and it is omitted. Amplification is within $3 \div 10$.

of every image (i.e., separated from proper brightness variations that are intrinsic to the source), which arises because of the source motion⁷. As before, for a theoretical treatment we deal with the amplification curves, that is the dependence of the amplification coefficients upon the time.

Our aim is to estimate the statistical effect of the extended masses (clumps) on the autocorrelation functions of the amplification curves. To compare the amplification curves in microlensing systems with a different content of these clumps, we consider a simple model of stochastic point and extended masses. We confine ourselves to a special case of the cored clumps according to Eq. (3) with $a = 2$ (cf. Zhdanov et al. (2012)). An external shear owing to the average field of the lensing galaxy will also be taken into account. Thus, we use the lens equation for N masses in one lens plane

⁷ which is again assumed to be a uniform straight line motion.

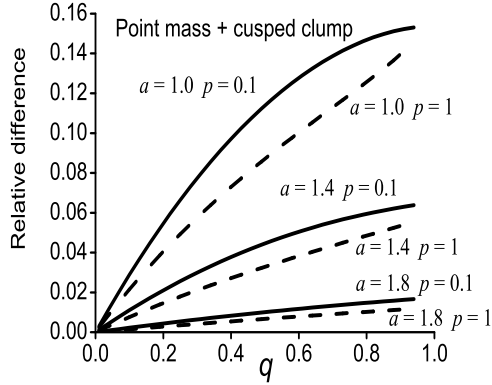


Figure 7. Relative differences δ of the amplification curves for different cusped clump contributions q in the microlensing complex "point mass + clump". Here $a = 1.0, 1.5, 1.8$. For the impact parameter $p = 0.1$ (solid) the amplification is within $\sim 10 \div 20$; for $p = 1$ (dashed) the amplification is $\sim 1.3 \div 2$. For $p = 0.03$ we have practically the same curves as for $p = 0.1$, but the amplification varies from ~ 30 to 60 .

$$\mathbf{y} = \hat{\mathbf{A}}\mathbf{r} - \sum_{i=1}^N \frac{R_{E,i}^2(\mathbf{r} - \mathbf{r}_i)}{|\mathbf{r} - \mathbf{r}_i|^2 + r_{s,i}^2} \quad (12)$$

where $\hat{\mathbf{A}} = \text{diag}\{1 - \gamma, 1 + \gamma\}$ is the two-dimensional external shear matrix (the optical depth of the background continuous matter is taken to be zero), $r_{s,i}$ is a characteristic size of the i -th cored clump with mass M_i , \mathbf{r}_i is the position of its center on the lens plane, and $R_{E,i}$ its Einstein ring radius: $R_{E,i}^2 = 4GM_i D_{ds} / (c^2 D_d D_s)$. Obviously, for $r_{s,i} = 0$ we have ordinary point microlenses with mass M_i .

In our simulations, the microlens masses and positions were chosen in a random way. The positions \mathbf{r}_i were distributed homogeneously inside a circle, which was big enough to minimize the boundary effects; also, to check the result convergency we considered different sizes of the circle. The mass distribution followed the Salpeter's law (Salpeter 1955) with a power-law index -2.35 within the mass range $M_i \in [0.4; 10]M_\odot$. In every set of numerical experiments, the input parameters (that were controlled to be the same in all the realizations of the set) were as follows: the total optical depth of the microlensing field σ_{tot} , the optical depths σ_p , σ_{cl} of the point masses and the extended clumps ($\sigma_{cl} + \sigma_p = \sigma_{tot}$), and the relative size of the clumps $\kappa = r_{s,i}/R_{E,i}$. To introduce the clumps into the microlensing field, we replaced some randomly chosen part of point masses by extended clumps without changing their positions \mathbf{r}_i , masses M_i ; the size parameter was $r_{s,i} = \kappa R_{E,i}$. Then, for each realization of the microlensing field we obtain an amplification map by means of the ray shooting method combined with our GPU-enabled microlensing C++ code based on the hierarchical tree algorithm (Schneider et al. 1992; Wambsganss et al. 1992). Convolution of the amplification map with the normalized brightness distribution over the initial source $I(\mathbf{y})$ yields the amplification coefficient μ . The mathematical representation of this procedure can be written as (Alexandrov & Zhdanov 2011; Zhdanov et al. 2012)

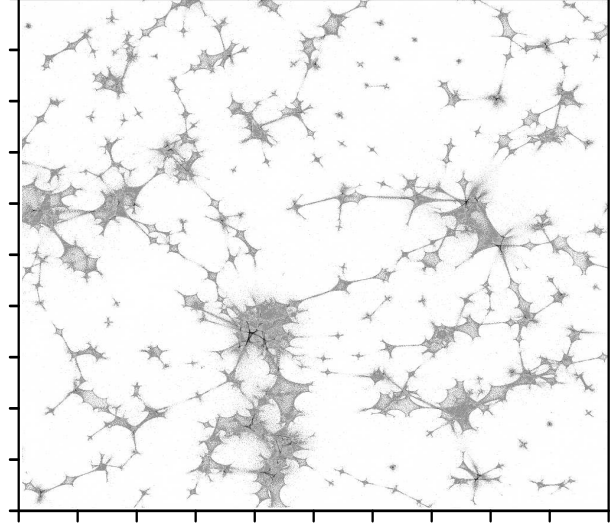


Figure 8. Amplification map for $\sigma_{cl} = 0, \gamma = 0, \sigma_{tot} = 0.3$.

$$\mu(\mathbf{y}) = \iint I[\mathbf{Y}(\mathbf{x}) - \mathbf{y}] dx_1 dx_2,$$

where \mathbf{y} is the position of the source center in the source plane and $\mathbf{y} = \mathbf{Y}(\mathbf{r})$ represents the lens mapping $\mathbf{r} \rightarrow \mathbf{y}$. We used a Gaussian model for $I(\mathbf{y})$; the source half-brightness radius was $R_{1/2} = 0.2$, its motion has been assumed to be uniform. Due to the motion of the source we have an amplification curve $\mu(t)$.

Having a large number of realizations of the microlensing field and the corresponding amplification curves $\mu(t)$, we have calculated the ACFs

$$A(\tau) = (\Delta\mu)^{-2} \langle [\mu(t) - \mu_0][\mu(t + \tau) - \mu_0] \rangle, \quad (13)$$

where

$$\mu_0 = \langle \mu(t) \rangle, \quad \Delta\mu = \sqrt{\langle [\mu(t) - \mu_0]^2 \rangle}, \quad (14)$$

the brackets $\langle \dots \rangle$ denote the averaging over all the realizations of the amplification curves for the fixed value of the optical depth of continuous masses σ_{cl} and point masses σ_p .

To consider the possible observational manifestations of the extended microlenses, their size R_c has been chosen to be comparable with a typical Einstein ring radius R_E of the microlenses; otherwise in the limiting situations we approach to either the well-known case of a continuous background matter for $R_c \gg R_E$, or we have a standard microlensing of point masses. Here we present the results for $\sigma_{tot} = 0.3$, and $\kappa = 5$. The parameter σ_{cl} has been varied from zero to 0.3. The length unit corresponds to $R_{E,\odot} = [4GM_\odot D_{ds} / (c^2 D_d D_s)]^{1/2} = 1$. Furthermore, t and τ are in units of $R_{E,\odot}$ (i.e. assuming a velocity $V = 1$); the normalization to M_\odot is just conventional.

The examples of the amplification maps in the source plane are shown in Figs. 8 - 10. The amplification distributions for various fractions of clumps (and the same $\sigma_{tot} = 0.3, \gamma = 0$) noticeably differ one from another. As can be expected, the presence of the clumps makes this distribution smoother. The presence of non-zero γ (Fig. 10) stretches the maps in the direction of the shear. For every set of parameters $\sigma_{tot}, \sigma_{cl}, \gamma$ we generated typically several hundred maps and the corresponding amplification curves.

Using the ensemble of these curves, the averaging procedure yields ACF $A(\tau)$. These functions are shown in Figs.

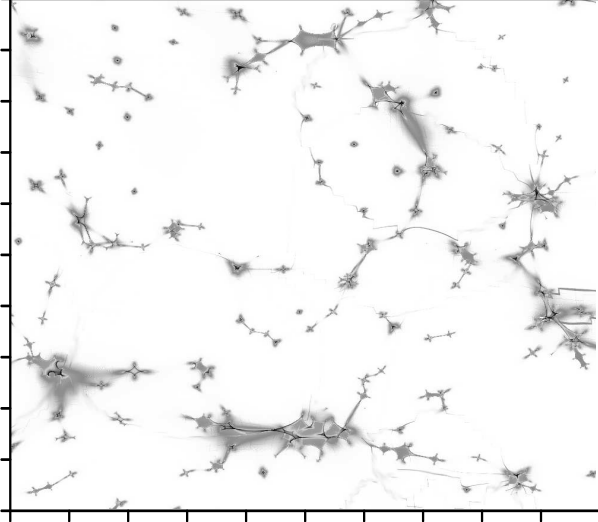


Figure 9. The amplification map for $\sigma_{cl} = 0.2, \gamma = 0$, here and below $\sigma_{tot} = 0.3$, and the size parameter is $\kappa = 5$.

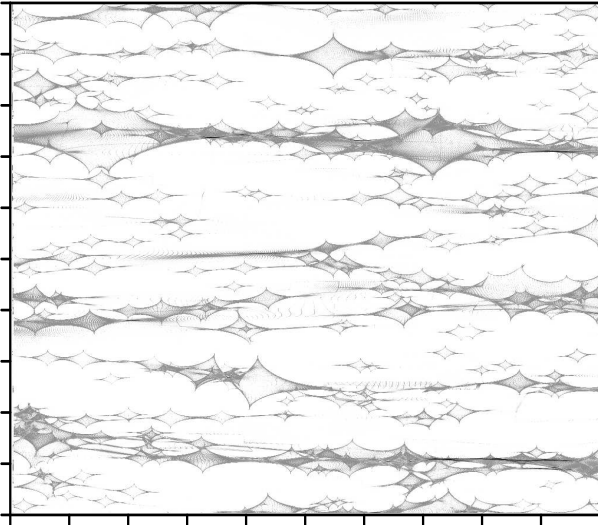


Figure 10. The amplification map for $\sigma_{cl} = 0.2, \gamma = 0.5$.

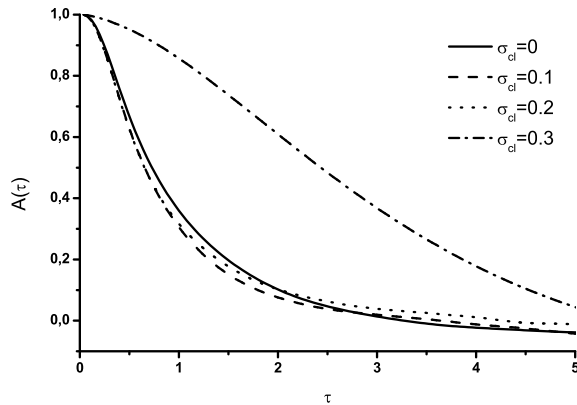


Figure 11. ACFs of the amplification curves for the case $\sigma_{tot} = 0.3, \kappa = 5, \gamma = 0$ and for $\sigma_{cl} = 0, 0.1, 0.2, 0.3$.

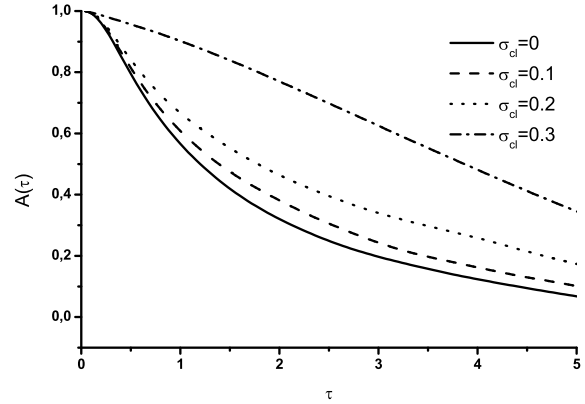


Figure 12. ACFs of the amplification curves for the case $\sigma_{tot} = 0.3, \kappa = 5, \gamma = 0.5$ and for $\sigma_{cl} = 0, 0.1, 0.2, 0.3$.

11, 12 for different fractions of point masses and clumps. We note that the behavior of $A(\tau)$ and $\Delta\mu$ as functions of σ_{cl} appears to be rather complicated. E.g., for $\gamma = 0$ we see a non-monotonic variation of the curves as σ_{cl} changes (Fig. 11). This effect is not observed for non-zero values of the shear (see the case $\gamma = 0.5$ in Fig. 12).

6 DISCUSSION

We have analyzed the observational signatures of gravitational microlensing in presence of extended masses (clumps), which can represent, for example, hypothetical structures arising in cold DM models as a result of clustering. To produce significant effects due to the presence of the clumps, the masses of the clumps were chosen of the same order as those of the point masses, and the sizes of the clumps were of the order of several typical Einstein radii. We compared the artificial amplification curves (essentially, the light curves) arising due to a relative motion of the microlens with respect to a remote source.

We have proposed simple models that describe circular symmetric cusped or cored clumps and their combinations with point masses. We do not consider these idealized models as the only possible ones, rather, our aim was to look at some "toy problems" in order to see the main qualitative features accompanying the microlensing process in our Galaxy and beyond in presence of small-scale DM clustering, and to estimate the order of the effects involved. We believe that our main findings on this matter will be preserved at a qualitative level for more complicated models of the DM clumps, though an exact final answer will be the subject of a separate investigation.

In case of Galactic microlensing, the case of isolated circular symmetric microlenses of Section 3 has led to a detailed analytical treatment; here the regions of parameters of the lens mapping yielding the occurrence of one, two or three images were determined. We note that any structures yielding changes in the number of images (cf. caustic crossings, occultations) are possible only in case of a considerable local dark matter density, either near the clump centers or around the point masses. The most vivid example is an eclipse-like effect with the total disappearance of the lensed images. Though, we do not believe this case to be realistic for the Galaxy conditions, we cannot exclude it at

all. It may be difficult to distinguish such complicated events from those related to double stars or planetary systems; here a detailed investigation of the light curves of concrete high amplification events (HAEs) is required.

We considered relatively simple models and events. We found that the light curve of a HAE in presence of the extended microlens (the isolated clump or its superposition with the point mass) can be well mimicked by a light curve of the Schwarzschild lens with appropriately chosen mass and parameters associated with its motion. Nevertheless, in case of such a fitting, there remain some residuals in the wings of the HAE light curve that can be used to distinguish between the microlens models. These residuals have been estimated through the fitting of the light curves of our clump model by those of the point mass lens (Sections 4.2, 4.3); these results determine the required level of photometric accuracy needed to detect the signals from the extended clumps. This level can be estimated from Figs. 6, 7. In particular, for cored clump + point mass system with $r_s = p = 1$ (that is, the core size and impact parameter are equal to the Einstein ring radius) and average values $q = 0.5, a = 1.5$ the light curve deviation from that of the ordinary point mass lens can be detected if the photometric accuracy is at the $\sim 0.02 \text{ mag}$ level. So is also the case of the cusped clump, and the requirements to the accuracy in case of a pure cusped or cored clump ($q = 1$) are even lower.

We also note that the degeneracy in the choice of the model can be reduced by simultaneous astrometric observations of the source image centroid motion (see Fig. 3). If this information is available, this may help to restrict the parameters of the microlensing system. Though this does not mean that all of them can be determined uniquely, not to mention the question of uniqueness of the microlensing model itself.

In any case, there is a region of the clump parameters that induces a considerable difference between the light curves, which is within the reach of modern photometric measurements. Therefore, we see that at least some extended microlens models can be, in principle, either confirmed or rejected from the use of high-quality observations. However, in real observations of microlensing by Galactic objects, the situation will be aggravated by the possible presence of unobservable planets and star companions. Then in this case a more detailed treatment of concrete high amplification events is also necessary to compare the models that involve binaries and planets with those dealing with extended clumps.

In extragalactic GLSs the situation is much more complicated. The view of amplification maps and the caustic network generated by simple point mass microlenses (i1) seems to be rather different from those in presence of a considerable contribution of extended clumps (i2). Nevertheless, individual light curves in case (i1) can also include high amplification and de-amplification effects which have an analogous look as in case (i2). The other complication in extragalactic GLSs is that owing to the non-negligible source size since both the light curves and the centroid brightness trajectory will be smoothed out significantly. To have an idea about microlensing in cases (i1) and (i2), we considered statistical models of many-body microlensing systems that involve both point and extended microlenses. The latter have been represented by a special case of the cored clumps.

Considerations of Section 5 have much in common with considerations by Metcalf & Madau (2001); Chiba (2002); Dalal & Kochanek (2002); Schechter & Wambsganss (2002) that, among other questions, deal with the issue of microlensing by extended structures. In particular, Schechter & Wambsganss (2002) pay attention to microlensing brightness variations in presence of a variable smooth matter depending on the parity of the close macrolens images. These papers, however, are mainly aimed at investigating the problem of anomalous flux ratios and therefore they deal with other mass and spatial scales. Our simulations deal with extended microlenses (e.g., DM clumps) of stellar mass, with sizes comparable to that of corresponding Einstein rings – in order to have a noticeable effect in the light curves. A technical difference of our simulations owes to the simplified model of the lens mapping in presence of the clumps, which enables us to speed up the numerical calculations of ACFs with a rather modest computer hardware. For every choice of parameters that characterize the content of the clumps, their sizes and masses, we generated an ensemble of amplification curves assuming a uniform spatial distribution of microlenses in the lens plane. Using these curves we built ACFs of the amplification curves for a set of optical depths of extended clumps and point masses. Joint use of microlensed flux variations and ACFs may provide a means for determining the clump fraction and the other parameters of the lensing system.

Indeed, there is a notable difference between the ACFs for different values of the clump contribution. In this view, we note the remark by Schechter & Wambsganss (2002) that the microlensing variations appear to be "less dramatic for extended subhalos than for point microlenses". This also has been mostly observed in our simulations, though with some exceptions. One could expect that by and large the extended structures make ACFs less steep and therefore, this effect shall increase the corresponding correlation length, and this typically is the case for $\sigma_{cl} \leq 0.3$ and $\gamma \in [0, 0.5]$ ($\sigma_{tot} = 0.3$), but also with some exceptions showing a complicated dependence of ACFs upon σ_{cl} (Figs. 11, 12).

However, detection of these effects requires sufficiently long observations of the light curves in real GLSs. The relevance of our results to extragalactic systems is connected also with the occurrence of a significant optical depth σ_{cl} . This depends on the surface mass density along the line-of-sight which is not well known. For very rough estimations one can use the masses and sizes of the galactic haloes as compared to those of the stellar population⁸. The density of DM in the Universe is five times higher than the baryonic one and the percentage of the luminous matter in galaxies is even lower by one order. Then, it may be quite possible to have the surface mass density of the extended clumps of some GLS of the same order as that of the point masses (stars). Moreover, despite the mass-luminosity ratio for typical galaxies is known to be at the level of $M/L \sim 2 - 4$, for some spherical dwarf galaxies it is $M/L \sim 100$ (Swaters et al. 2011).

⁸ see, e.g., the examples from Shull (2014)

7 CONCLUSIONS

To sum up, we studied microlensing of a remote source by point and extended masses, the latter representing hypothetical results of cold DM clustering. In case when the masses of the extended clumps are comparable to those of the point objects (stars) and their characteristic sizes are of the same order as the Einstein radius of the stars, our findings are as follows:

- We proposed a simple circular symmetric model of microlensing by isolated dark matter clumps that allowed us a detailed investigation of the corresponding lens mapping.

- In case of a single point source motion, we built amplification curves of the lensed images; this is done in case of microlensing by the isolated clumps and/or concentric clumps and point masses. For a wide range of model parameters, we estimated the residuals after fitting these amplification curves with those due to the single point mass microlensing.

- The results allow one to estimate the photometric accuracy needed to differentiate the model with the extended clumps and without them. We note that a number of model parameters can be ruled out under the level of photometric accuracy $\Delta m = 0.01 - 0.02$.

- In case of extragalactic gravitational lens systems, we built autocorrelation functions of the amplification curves for different clump contributions. We found a noticeable difference between ACFs in case of a considerable value for the clump contribution and without the clumps.

8 ACKNOWLEDGEMENTS

We thank the anonymous referee for her/his helpful comments. EF acknowledges the AGO/AEOS Institute of Astrophysics and Geophysics of Liège University for their warm hospitality and providing the technical facilities for this work. EF and JS acknowledge support from the ESA PRODEX programme “Gaia-DPAC”, and from the Belgian Federal Science Policy Office. VIZ acknowledges partial support from the State Fund for Fundamental Research of Ukraine, project $\Phi 64/42-2015$. This work has been supported in part by the scientific program “Astronomy and Space Physics”, Taras Shevchenko National University of Kyiv.

REFERENCES

- Ade P. A. R. et al. 2013 *A&A* **1303**, 5062.
 Alcock C., Akerlof C. W., Allsman R. A., et al., 1993, *Nat*, **365**, 621.
 Alexandrov A.N., Zhdanov V.I., 2011, *MNRAS*, **417**, 541.
 Aubourg E.; Baryshev P.; Bréhin S. E. et al., 1993, *Nat*, **365**, 623.
 Baryshev Yu., Bukhmastova Yu. 1997, *Astron.Rep.*, **41**, 436.
 Berezhinsky V., Dokuchaev V., Eroshenko Yu. 2008, *Phys.Rev.D*, **77**, 083519.
 Berezhinsky V., Dokuchaev V., Eroshenko Yu. 2013, *JCAP*, **11**, 059.
 Bradač M., Clowe D., Gonzalez A. H. et al. 2006, *ApJ*, **652**, 937.
 Chen J. et al. 2007, *ApJ*, **652**, 52.
 Chiba M. 2002 *ApJ*, **565**, 17.
 Clowe D., Gonzalez A., & Markevitch M. 2004, *ApJ*, **604**, 596
 Clowe D., Bradač M., Gonzalez A. H. et al. 2006, *ApJL*, **648**, L109.
 Congdon A., Keeton C., Nordgren C. 2010, *Aph.J.*, **709**, 552.
 Contini E., De Lucia G., Borgani S. 2012, *MNRAS*, **420**, 2978.
 Dalal N., Kochanek C. S. 2002, *ApJ*, **572**, 25.
 Del Popolo A. 2014, *Int.Journ. Mod. Phys. D*, **23**, N3, 1430005.
 Del Popolo A., Lima J. A. S., Fabris J. C., Rodrigues D.C. 2014, *JCAP*, **4**, id.21
 Diemand J., Moore B., Stadel J. 2004, *MNRAS*, **352**, Is. 2, 535.
 Diemand J., Moore B., Stadel J. 2005, *Nature*, **433**, 389-391.
 Dobler G., Keeton C.R., Wambsganss J. 2007, *MNRAS*, **377**, 977-986.
 Fedorova E., Del Popolo A., Zhdanov V.I., Alexandrov A.N., Sliusar V. 2014, *Rencontres de Moriond 49th. Cosmology*, Eds: E.Auge, J.Dumarchez and J. Tran Thanh Van al. La Thuile 2014 Proceedings, 407.
 Jeans J. 1923, *MNRAS*, **84**, 60.
 Hisano J., Inoue K.T., Takahashi T. 2006, *Phys.Lett.B.*, **643**, 141.
 Kains, N.; Street, R. A.; Choi, J.-Y.; Han, C.; Udalski, A. et al. 2013, *A&A*, **552**, id.A70, 10 pp.
 Kapteyn J.C. 1922, *Aph.J.* **55**, 302.
 Keeton C.R., Moustakas L.A. 2009, *ApJ*, **699**, 1720.
 Klypin A., Kravtsov A., Valenzuela O., Prada F. 1999, *Aph.J.*, **522**, 82.
 Knebe A., Arnold B., Power C., Gibson B.K. 2008, *MNRAS*, **386(2)**, 1029.
 Knebe A., Devriendt J., Gibson B., Silk J. 2003, *MNRAS*, **345**, 1286.
 Kormendy J, Freeman K.C. 2003, *IAU Symp.220 Eds: S.D.Ryder et al. San Francisco: Astron. Soc. Pacific.*, 377; astro-ph/0407321.
 Lee S.K. Ando A., Kamionkowski M. 2009, *JCAP*, **07**.
 Markevitch M., Gonzalez A., Clowe D. et al. 2003, *Aph.J.*, **606**, 819.
 MacLeod C. et al. 2013, *Aph.J.*, **773**, 35.
 Mao S., Jing Y., Ostriker J. P., Weller J. 2004, *ApJ*, **604**, L5.
 McKean J. P. et al. 2007, *MNRAS*, **378(1)**, 109.
 Metcalf R.B., Madau P., 2001, *ApJ* **563**, 9.
 Metcalf R.B., Moustakas L. A. Bunker A. J., Parry I. R. 2003, *Aph.J.* **607(1)**, 43.
 Moore B. et al. 1999, *Aph.J.*, **524**, L19.
 Navarro J., Frenk C., White S. 1996, *ApJ*, **462**, 563.
 Neindorf B., 2003, *A&A*, **404**, 83.
 Oguri M. 2005, *MNRAS*, **361(1)**, L38.
 Oort J.H., 1932, *Bull. Astron. Inst. Netherlands*, **6**, 249.
 Öpik E. 1915, *Bull. de la Soc. Astr. de Russie* **21**, 150.
 Paczyński B. 1986, *Aph.J.* **301**, 503.
 Paczyński B. 1986, *Aph.J.* **304**, 1.
 Paczyński B., Wambsganss J. 1989, *ApJ* **337**, 581.
 Paduroiu S., Revaz Y., Pfenniger D. 2015, *ArXiv* 1506.03789.

- Riess A.G., Casertano S., Anderson J., MacKenty J., Filippenko A. 2014, *Aph.J.*, **785(2)**, 161.
- Rocha M.E. et al. 2012, *MNRAS*, **430(1)**, 81.
- Salpeter E., 1955, *ApJ*, **121**, 161.
- Schechter P., Wambsganss J. 2002, *AJ*, **580**, 685.
- Schneider P., Ehlers J., and Falco E. E., *Gravitational Lenses*, Springer, New York, NY, USA, 1992.
- Schneider A., Krauss L., Moore B. 2010, *Phys.Rev.D*, **82**, 063525.
- Schneider A., Krauss L., Moore B. 2011, *ArXiv* 1105.4106.
- Schneider A., Smith R.E., Macci A., Moore B. 2012, *MNRAS*, **424**, 684.
- Schneider P., Weiss A., 1987, *MPA Rep.*, **311**, 46.
- Schmidt R. W., Wambsganss J., 2010, *GRG* **42**, 2127.
- Shaw L. D., Weller J., Ostriker J.P., Bode P. 2007, *Aph.J.*, **659**, 1082.
- Seitz C., Schneider P. 1994, *A&A* **288**, 1.
- Shin I.-G.; Han C.; Choi J.-Y. et al. 2012, *Aph.J.*, **755**, id. 91, 10 pp.
- Shull J.M. 2014, *Aph.J.*, **784**, Is. 2, 10.
- Sliusar V.N., Zhdanov V.I., Alexandrov A.N., Fedorova E.V. 2015, *Kinemat. Phys. Celest. Bodies* **31**, Is. 2, 47.
- Springel V. et al. 2005, *Nature*, **435**, 629.
- Springel V., Wang J., Vogelsberger M. et al. 2008, *MNRAS*, **391**, 1685.
- Stadel J., Potter D., Moore B., et al. 2009, *MNRAS*, **398**, L21.
- Swaters R.A., Sancisi R., van Albada T.S., van der Hulst J.M. 2011, *Aph.J.*, **729**, DOI:10.1088/0004-637X/729/2/11.
- Tisserand P., Le Guillou L., Afonso C., et al. 2007, *A&A*, **469**, 387.
- Udalski A., Szymański M., Kaluźny J., et al. 1993, *Acta Astron.*, **43**, 289.
- Wambsganss, J., Paczyński, B., Katz, N. 1990, *Aph.J* **352**, 407.
- Wambsganss J., Witt H.J., Schneider P. 1992, *A&A*, **258**, 591.
- Wyzykowski L., Kozłowski S., Skowron J., et al., 2009, *MNRAS*, **397**, 1228.
- Vogelsberger M. et al. 2012, *MNRAS*, **423**, 3740.
- Zackrisson E., Riehm T. 2010, *Advances in Astronomy*, id. 478910.
- Zakharov A. 2010, *Gen.Rel.Grav.*, **42**, 2301.
- Zakharov A.F., Sazhin M.V. 1999, *A&AT*, **18**, 27.
- Zhdanov V., Alexandrov A., Fedorova E., Sliusar V. 2012, *ISRN A&A*, **2012**, ID 906951.
- Zhang D. 2011, *MNRAS*, **418(3)**, 1850.
- Zwicky F. 1933, *Helvetica Physica Acta*, **6**, 110.

APPENDIX A: FITTING THE AMPLIFICATION CURVE IN CASE OF A SCHWARZSCHILD LENS

In case of a point mass (Schwarzschild) lens we have the mapping

$$\mathbf{y} = \mathbf{r} \left(1 - \frac{R_E^2}{r^2} \right) \quad (\text{A1})$$

The amplification is well known:

$$\mu(\mathbf{y}) = \frac{y^2 + 2R_E^2}{y\sqrt{y^2 + 4R_E^2}}. \quad (\text{A2})$$

In case of a relative straight-line motion of the lens and the source we have $y^2/R_E^2 = p_S^2 + V_S^2 t^2$, V_S is the velocity, p_S is the impact parameter. Therefore, the problem of fitting any given dependence $\mu(t)$ (e.g., that has been obtained for a clumped or cusped lens model) by means of (A2) is reduced to finding the coefficients a, b of an approximate linear mapping $t^2 \rightarrow y$:

$$a + bt^2 = 2 \left(\frac{\mu(t)}{\sqrt{\mu^2(t) - 1}} - 1 \right), \quad (\text{A3})$$

where $a = p_S^2$, $b = V_S^2$. Obviously, p_S and V_S will differ from that of the initial clump model. In our case, to estimate the difference between models, the approximation is performed near the maximum of the amplification curve, where it has a parabolic form (typically for $|t| < 0.05$. Here residuals of the approximation are of the order of $10^{-5} \div 10^{-8}$). Using the point mass model with the parameters obtained as the result of this approximation, we estimated δ for a larger interval.

Note that to determine p_S and V_S we deal with the relative values y/R_E irrespective of R_E , which is not essential for fitting the amplification. However, this is essential when considering the image centroid. E.g., in case of two images, the image centroid is

$$\mathbf{r}_c = \frac{\mu_1 \mathbf{r}_1 + \mu_2 \mathbf{r}_2}{\mu_1 + \mu_2},$$

where \mathbf{r}_i is the i -th image position and μ_i is its amplification ($i = 1, 2$). Here we have an additional parameter R_E that can be used to rescale the trajectory $\mathbf{r}_c(t)$; this is done in the lower panel of Fig. 3.